

Minimax Isometry Method

Merzuk Kaltak* and Georg Kresse†
(Dated: May 2, 2022)

We present a compressive sensing approach for the long standing problem of Matsubara summation in many-body perturbation theory. By constructing low-dimensional, almost isometric subspaces of the Hilbert space we obtain optimum imaginary time and frequency grids that allow for extreme data compression of fermionic and bosonic functions in a broad temperature regime. The method is applied to the random phase and self-consistent *GW* approximation of the grand potential and integration and transformation errors are investigated for Si and SrVO₃.

Keywords: MP2, RPA, Laplace transformed MP2, imaginary time, imaginary frequency, Minimax approximation, non-uniform cosine transformation, Low scaling RPA algorithm, finite temperature, grand canonical ensemble, RPA and metals, Matsubara summation, compressive sensing, almost isometry, epsilon isometry

I. INTRODUCTION: MATSUBARA TECHNIQUE

The Matsubara technique is a way to formulate quantum field theory at finite-temperature. More precisely, it makes use of the Wick rotation¹, which transforms the real time axis of Minkowski spacetime to the imaginary time axis $t \rightarrow -i\tau$. Because real space remains unchanged by this transformation, spacetime becomes essentially euclidean, so that this approach is also known as euclidean quantum field theory (QFT). A summary on euclidean QFT is given in the appendix. Here we focus on the Matsubara method.

As Matsubara has shown, the imaginary time-integrals in finite-temperature perturbation theory are restricted to the interval $-\beta < \tau < \beta$.² This has the advantage that one can expand the imaginary time-dependence of the corresponding integrands into a Fourier series, such that imaginary-time integration becomes essentially an (infinite) series over discrete Fourier coefficients. The corresponding discrete frequencies are known as *Matsubara frequencies* and it is important for us to distinguish between *fermionic*, denoted by ω_n in the following, and *bosonic* Matsubara frequencies, denoted by ν_m in the remainder of this paper.

Fermionic Matsubara frequencies represent the non-zero Fourier modes of fermionic functions, while bosonic frequencies are the non-zero modes of bosonic functions. This is explained in more detail below by means of the free-electron Green's function (Feynman propagator) and the irreducible polarizability, the building blocks of finite-temperature perturbation theory.

The free Feynman propagator in imaginary time $-i\tau$ represents a prototype of a fermionic function. In a one-electron basis the free propagator is diagonal $g_{\alpha\gamma}(-i\tau) = \delta_{\alpha\gamma}g_{\alpha}(-i\tau)$ and the entries read^{3,4}

$$g_{\alpha}(-i\tau) = e^{-(\epsilon_{\alpha} - \mu)\tau} [(1 - f_{\alpha})\Theta(\tau) - f_{\alpha}\Theta(-\tau)], \quad (1)$$

where ϵ_{α} , μ and f_{α} are the one electron energy, the chemical potential and the Fermi function (see Equ. A10), respectively. Here Θ is the Heaviside step function,⁵ and it is the reason why $g_{\alpha}(-i\tau)$ changes sign at $\tau = 0$. Also,

the presence of the step functions implies

$$g_{\alpha}(-i\beta + i\tau) = -g_{\alpha}(i\tau), \quad 0 < \tau < \beta. \quad (2)$$

This anti-symmetric property has an important effect on the Fourier series in the interval $-\beta < \tau < \beta$

$$g_{\alpha}(-i\tau) = \frac{1}{\beta} \sum_{m=-\infty}^{\infty} \tilde{g}_{\alpha}(i\omega_m) e^{-i\omega_m\tau} \quad (3)$$

$$\tilde{g}_{\alpha}(i\omega_m) = \int_{-\beta/2}^{\beta/2} d\tau g_{\alpha}(-i\tau) e^{i\omega_m\tau}, \quad (4)$$

because it contains only fermionic frequencies

$$\omega_m = \frac{2m+1}{\beta}\pi, \quad m \in \mathbb{Z}. \quad (5)$$

This holds true for all fermionic functions on the imaginary time axis, including the self-energy (see appendix B).

An example for a bosonic function is the independent particle polarizability, which is diagonal $\chi_{\alpha\gamma\alpha'\gamma'} = \delta_{\alpha\alpha'}\delta_{\gamma\gamma'}\chi_{\alpha\gamma}$ and has the entries

$$\chi_{\alpha\gamma}(-i\tau) = -g_{\alpha}(-i\tau)g_{\gamma}(+i\tau). \quad (6)$$

However, in contrast to Equ. (2), bosonic functions do not change sign in imaginary time, but are symmetric

$$\chi_{\alpha\gamma}(-i\beta + i\tau) = \chi_{\alpha\gamma}(+i\tau), \quad 0 < \tau < \beta. \quad (7)$$

Consequently, the Fourier expansion

$$\chi_{\alpha\gamma}(-i\tau) = \frac{1}{\beta} \sum_{n=-\infty}^{\infty} \tilde{\chi}_{\alpha\gamma}(i\nu_n) e^{-i\nu_n\tau} \quad (8)$$

$$\tilde{\chi}_{\alpha\gamma}(i\nu_n) = \int_{-\beta/2}^{\beta/2} d\tau \chi_{\alpha\gamma}(-i\tau) e^{i\nu_n\tau} \quad (9)$$

contains only bosonic frequencies

$$\nu_n = \frac{2n}{\beta}\pi, \quad n \in \mathbb{Z}. \quad (10)$$

It is often argued that bosonic (fermionic) functions are periodic (anti-periodic) in τ . This is strictly speaking

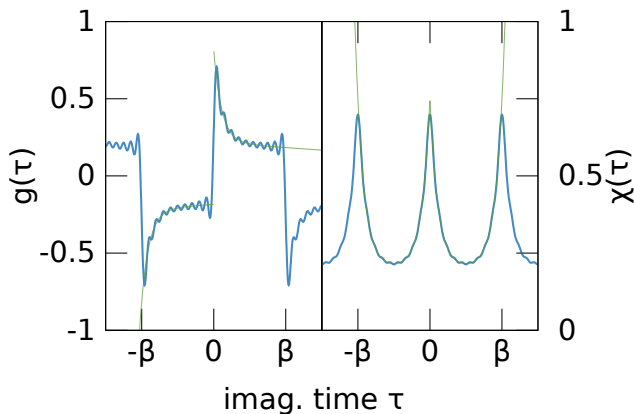


FIG. 1. (left) Fermionic function $g_1 + g_2$ with $\epsilon_1 = 0.19$, $\epsilon_2 = 9.12$ eV and $\beta = 1$ eV $^{-1}$ in the fundamental interval (green line) and its corresponding Fourier series truncated after $m > 10$ (blue line). (right) Corresponding bosonic function. Analytic fermionic and bosonic functions either increase or decrease exponentially for $|\tau| > \beta$ (e.g. Equ. (1)), while the corresponding Fourier expansion outside $[-\beta, \beta]$ is (anti-)periodic.

not correct. The free propagator, for instance, is defined *a priori* only in the fundamental imaginary time interval $|\tau| \leq \beta$, because (1) grows or decays exponentially for arguments outside (green lines in Fig. 1). The same holds true for the irreducible polarizability. In fact, only the Fourier expansions (8) and (3) define periodic and anti-periodic functions in τ with (anti-) period β . This behavior is illustrated in Fig. 1 showing a typical fermionic and bosonic function. In practice, it is quite important to recall that exponentially growing terms in propagators are not present, because the τ -integrations are performed over $0 < \tau < \beta$ or, equivalently, over $-\beta/2 < \tau < \beta/2$. Due to consistency with our previous papers⁶⁻⁸ we work in the $[-\beta/2, \beta/2]$ interval. Furthermore, we mean by correlation function either a bosonic or fermionic function.

The Matsubara summation has one major drawback. Matsubara series converge very slowly with the cutoff frequency, as shown in IID. One thus requires compressed Matsubara representations of bosonic and fermionic correlation functions. For this purpose we studied isometries in metric spaces and developed the following formalism.

II. MINIMAX ISOMETRY

To keep the notation simple, we consider the case $\beta = 1$ eV $^{-1}$ in the following. The general case $\beta \neq 1$ follows from scaling relations that are discussed in IIB and IIC.

Deriving an alternative to the Matsubara technique requires one additional abstraction level. For this purpose we write x for the energies $\epsilon_\alpha - \mu$ and assume that $a \leq x \leq b$ ($b \rightarrow \infty$ is allowed in the following). Every energy x is represented by a vector $|x\rangle$ in a Hilbert space

\mathcal{H} and it is assumed that $|\tau\rangle$ and $|n\rangle$ are two complete basis sets in imaginary time and frequency, such that the identity operator $\mathbb{1}$ can be expressed as

$$\mathbb{1} = \int_0^{1/2} d\tau |\tau\rangle \langle \tau| \quad (11)$$

$$\mathbb{1} = \sum_{n \in \mathbb{Z}} |n\rangle \langle n| \quad (12)$$

for all $x \in [a, b]$ with \mathbb{Z} representing the set of integers. From a functional analysis perspective, one says that the two spaces $\mathcal{U} = \text{span}\{|\tau\rangle\}_{\tau \in [0, 1/2]}$ and $\mathcal{V} = \text{span}\{|n\rangle\}_{n \in \mathbb{Z}}$ are isometric w.r.t. to the scalar product induced norm $\|x\|_2 = \sqrt{\langle x|x \rangle}$. This isometry is effectively a simple basis transformation that does not change the induced norm, since

$$\begin{aligned} \|x\|_2^2 = \langle x|x \rangle &= \int_0^{1/2} d\tau \langle x|\tau\rangle \langle \tau|x \rangle \\ &= \sum_{n \in \mathbb{Z}} \langle x|n\rangle \langle n|x \rangle. \end{aligned} \quad (13)$$

If $|\tau\rangle$ is the time and $|n\rangle = |\omega_n\rangle$ the frequency basis, then $\langle \tau|n\rangle$ and $\langle n|\tau\rangle$ are the matrix elements of the forward and backward basis transformation, respectively as for instance given in Eqs. (3),(4),(8) and (9).⁹ Consequently, the two spaces \mathcal{U} and \mathcal{V} are equivalent and span the same Hilbert space \mathcal{H} . This equivalence holds true only if infinitely many basis vectors are considered; for finite dimensional subspaces the perfect isometry (13) is violated.

One may illustrate the violation of the isometry (13) with the discrete Fourier transform (DFT) having the bases $|\tau_k\rangle = |\frac{1}{2N}(k - \frac{1}{2})\rangle$ with $(k = 1, \dots, N)$ and $|n\rangle = |2\pi(n - 1)\rangle$ (truncated bosonic Matsubara grid). The corresponding completeness relations (11), (12) become projectors onto finite dimensional subspaces $U \subset \mathcal{U}$, $V \subset \mathcal{V}$ and have the form

$$P = \frac{1}{2N} \sum_{k=1}^N |\tau_k\rangle \langle \tau_k| \quad (14)$$

$$\tilde{P} = \sum_{n=-N}^N |n\rangle \langle n|. \quad (15)$$

Only in the limit $N \rightarrow \infty$ the projectors approach the identity operator $\mathbb{1}$. For finite N , the isometry (13) is violated, but can be replaced by a so-called ε -isometry^{10,11}

$$\|P - \tilde{P}\|_\infty := \max_{a \leq x \leq b} |\langle x|P - \tilde{P}|x \rangle| \leq \varepsilon. \quad (16)$$

In the following, we will drop the subscript and write $\|\cdot\|$ for the maximum norm $\|\cdot\|_\infty$.

Of interest to us is the magnitude of ε and especially how it decreases with increasing N . For instance, in the case of the DFT $\langle x|P|x \rangle$ is the Riemann sum of the integral in (13) of order N and is known to be a poor method

to evaluate integrals. As a consequence, ε of the Matsubara grid is a weakly decaying function in N and cannot be used for our purposes, as shown in section II E.

The following question naturally arises: how can one determine ε -isometric subspaces $U = \text{span}\{|\tau_k\rangle\}_{k=1}^N$, and $V = \text{span}\{|\omega_k\rangle\}_{k=1}^N$, such that the completeness relations (11) and (12) are approximated as good as possible for all vectors $|x\rangle$ with $a \leq x \leq b$?

Using the notation in (16), the answer to this question are the solutions of following minimax problems:

$$\min_{\sigma_k > 0, \tau_k \in [0, 1/2]} \left\| \mathbb{1} - \sum_{k=1}^N \sigma_k |\tau_k\rangle \langle \tau_k| \right\| \quad (17)$$

$$\min_{\lambda_k > 0, \omega_k > 0} \left\| \mathbb{1} - \sum_{k=1}^N \lambda_k |\omega_k\rangle \langle \omega_k| \right\|. \quad (18)$$

Provided the solutions exist, they are known to yield errors ε that decay exponentially with N .¹² In the following we prove that (17) and (18) satisfy our requirements.

To prove the assertion above it suffices to show that the minimax errors are an upper bound for the isometry violation in (16). Therefore, assume $\{\sigma_k^*, \tau_k^*\}_{k=1}^N$ and $\{\lambda_k^*, \omega_k^*\}_{k=1}^N$ are the solutions of (17) and (18) and $P^* = \sum_{k=1}^N \sigma_k^* |\tau_k^*\rangle \langle \tau_k^*|$ and $\tilde{P}^* = \sum_{k=1}^N \lambda_k^* |\omega_k^*\rangle \langle \omega_k^*|$ the corresponding projectors, respectively. Then a positive number $\varepsilon/2$ exists (for every given N) as an upper bound for (17) and (18) and one can write

$$\begin{aligned} \left\| \mathbb{1} - P^* \right\| &\leq \frac{1}{2} \varepsilon \\ \left\| \mathbb{1} - \tilde{P}^* \right\| &= \left\| \tilde{P}^* - \mathbb{1} \right\| \leq \frac{1}{2} \varepsilon. \end{aligned} \quad (19)$$

Adding both inequalities in (19) and using the triangle inequality $\|f+g\| \leq \|f\| + \|g\|$ (satisfied by every norm¹³) one obtains

$$\underbrace{\left\| \mathbb{1} - P^* \right\| + \left\| \tilde{P}^* - \mathbb{1} \right\|}_{\left\| \mathbb{1} - P^* + \tilde{P}^* - \mathbb{1} \right\|} \leq \varepsilon. \quad (20)$$

Last inequality implies (16) for the projectors P^* , \tilde{P}^* and concludes our proof. \square

This is a quite remarkable result, because it means that the projectors P and P^* converge to the identity operator and, thus, define ε -isometric topological vector spaces U^* , V^* that have the *approximation property*.¹⁴ A summary of ε -isometric bases is given in Tab. I and its selection is motivated below.

Note that the discussion above does not give a prescription how to determine the transformation $U^* \rightarrow V^*$; a corresponding method is presented in section II E.

The proof above contains only an upper bound for the transformation error in (20). This upper bound ε is inherited from the sum of the convergence rate of the minimax solutions in the τ - and ω -domain. This convergence rate has been studied by Braess and Hackbusch

TABLE I. Almost isometric basis functions $\langle \omega|x\rangle$ and $\langle \tau|x\rangle$ related by cosine (subscript 1) or sine transformations (subscript 2). IA₁ and IB₂ represent bosonic (b) functions, whereas IA₂ and IB₁ represent fermionic (f) functions. $\langle \omega|x\rangle$ must be evaluated at the respective Matsubara grids. Third column shows the corresponding conserved L^2 -norm for $N \rightarrow \infty$ (given by Equ. (13)). From the infinite set of basis functions a discrete set with time points $\{\tau_j^*\}_{j=1}^N$ and frequency points $\{\omega_k^*\}_{k=1}^N$ will be selected to independently minimize the errors in the L^2 -norm tabulated in the column $\|x\|_2^2$.

group		$\langle \tau x\rangle$	$\langle \omega x\rangle$	$\ x\ _2^2$
IA ₁	b	$\frac{1}{2} \frac{\cosh \frac{x}{2} (1-2 \tau)}{\cosh \frac{x}{2}}$	$\frac{x \tanh \frac{x}{2}}{x^2 + \omega^2}$	$\tanh \frac{x}{2} + \frac{1 - \tanh^2 \frac{x}{2}}{8}$
IA ₂	f	$\frac{\text{sgn}(\tau)}{2} \frac{\cosh \frac{x}{2} (1-2 \tau)}{\cosh \frac{x}{2}}$	$\frac{\omega}{x^2 + \omega^2}$	
IB ₁	f	$\frac{1}{2} \frac{\sinh \frac{x}{2} (1-2 \tau)}{\cosh \frac{x}{2}}$	$\frac{x}{x^2 + \omega^2}$	$\tanh \frac{x}{2} - \frac{1 - \tanh^2 \frac{x}{2}}{8}$
IB ₂	b	$\frac{\text{sgn}(\tau)}{2} \frac{\sinh \frac{x}{2} (1-2 \tau)}{\cosh \frac{x}{2}}$	$\frac{\omega \tanh \frac{x}{2}}{x^2 + \omega^2}$	
IC ₁	b	$\frac{1}{2} e^{- x\tau }$	$\frac{ x }{x^2 + \omega^2}$	$\frac{1}{4x}$
IC ₂	f	$\frac{\text{sgn}(\tau)}{2} e^{- x\tau }$	$\frac{\omega}{x^2 + \omega^2}$	

for the minimax problem IC in the τ -domain listed in Tab. I. They obtained $\varepsilon(N) \approx 6.7 \log(2+N) e^{-\pi\sqrt{2N}}$ for $x \in [1, R_N]$, where $[1, R_N]$ belongs to the largest possible error for a given order N .¹⁵ Our numerical experiments discussed in section IV indicate similar convergence rates for all other minimax problems in Tab. I. In contrast, the DFT or Matsubara grid has only a linear rate of convergence $\varepsilon(N) \propto N^{-1}$.

A. Motivation of basis functions

In this subsection, we motivate our choice of ε -isometric basis functions tabulated in Tab. I. We start with the IC bases, which has been used in previous publications by the authors to construct optimized minimax grids for low scaling random phase and *GW* algorithms at zero temperature.⁶⁻⁸ Specifically, $\langle \tau|x\rangle$ of IC₁ describes the imaginary time dependence of the independent particle polarizability at zero temperature, while the corresponding ω -basis functions describe its imaginary frequency dependence.⁶ Then isometric bases are the ideal choice for the zero-temperature formalism of quantum field theory, because the corresponding conserved L^2 -norm (forth column of Tab. I) is the key quantity for the second order contributions to the correlation energy (see appendix (B1) or Ref. 6 and 16). These contributions involve energy denominators of the form $1/(\epsilon_a + \epsilon_b - \epsilon_i - \epsilon_j)$ and are considered to be bound, *i.e.* virtual states with energies ϵ_a, ϵ_b are separated by a band gap Δ from occupied states with energy ϵ_i, ϵ_j . The induced norm is

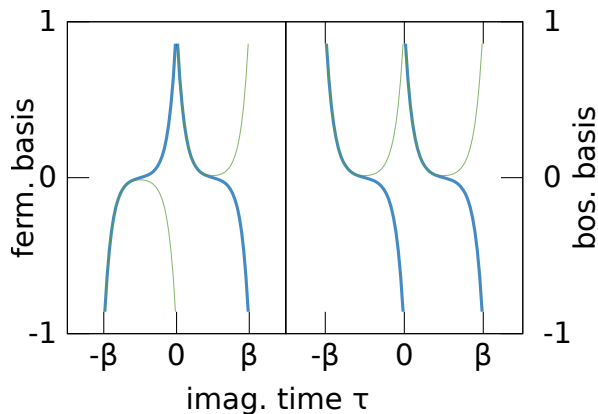


FIG. 2. (left) Fermionic basis functions $\langle \tau|x \rangle$ IA₂ (green line) and IB₁ (blue line) in imaginary time for $x = 10$. (right) Corresponding bosonic basis functions IA₁ (green) and IB₂ (blue).

important and essentially tells the optimization in the minimax problem, which contributions to the energy are most relevant. In our case contributions from small energy differences dominate over contributions from large energy differences.

The τ -basis function of IC₂ has the same time dependence (apart from the opposite sign), while the imaginary frequency dependence of the cosine transformation differs considerably from the one obtained from the sine transform (compare $\langle \omega|x \rangle$ of IC₁ and IC₂). It comes with no surprise that the corresponding minimax grids for τ and ω differ too.⁸ However, the minimax isometry guarantees that one can map in time between IC₁ and IC₂ with high precision; a fact that has been exploited in a low scaling self-consistent *GW* approach at zero temperature.¹⁷

Next, we consider the four basis functions of group IA and IB. They can be grouped into bosonic (IA₁ and IB₂) and fermionic (IA₂ and IB₁) pairs, where the ω -bases for bosonic (fermionic) functions are defined for bosonic (fermionic) frequencies *a priori* (see next section for additional motivation of these functions). The symbol $\langle \omega|x \rangle$ denotes the Fourier transformations (cosine or sine) of these functions. When optimizing the frequency grids using the minimax algorithm, we allow ω in IA and IB to deviate from the corresponding Matsubara grid. Indeed, the corresponding Minimax solutions are non-uniformly distributed, but nevertheless closely match Matsubara frequencies at small ω . It turns out, as shown in section IV, that this freedom allows us to describe the high frequency behavior of the correlation functions with high precision even in low dimensional subspaces U^* , V^* . The corresponding ε -isometric time basis functions have the fermionic anti-symmetry [Equ. (2)] and bosonic symmetry [Equ. (7)] for $-\beta/2 \leq \tau \leq \beta/2$, respectively, and are illustrated in Fig. 2.

Similar to the zero-temperature case, the conserved L^2 -norm describes the second order contribution to the correlation part of the grand-canonical potential (see ap-

pendix B1). Thus, it can be employed for data compression when calculating the correlation part of the grand canonical potential in the random phase approximation (see appendix B). The corresponding imaginary time and frequency grid are discussed in II B and II C, respectively.

There is one further important point to note here. Some bosonic functions, such as the polarizability or screened potential can be entirely presented by IA₁ basis functions since $\chi(-i\tau) = \chi(-i\beta + i\tau)$ (green lines in Fig. 2 right). This means that the second order part of the grand-canonical potential or the RPA correlation energy can rely on grids constructed for IA₁, only. This is not necessarily so for bosonic functions constructed e.g. by the product of the self-energy and Green's functions, as is the case in the Galitskii-Migdal (GM) formula.

In fact, the minimax isometry method is not straightforwardly applicable to the GM formula of the grand canonical potential; here both, even and odd basis functions in the frequency domain (IB₁ and IA₂) contribute to the grand potential and have different L^2 -norms (compare third column of IA and IB). We, therefore, propose an alternative approach in this case that is based on the minimization of the L^1 -quadrature error instead (see section IID).

B. Imaginary time grid

To construct an imaginary time grid, we make use of the scaling properties

$$\tau_j \rightarrow \beta\tau_j, \quad \sigma_j \rightarrow \beta\sigma_j \quad (21)$$

that allow to recover the time quadrature for an arbitrary interval $[0, \beta/2]$ from the unscaled solution determined for $[0, 1/2]$. Furthermore, we allow for infinitesimal small excitation energies $x = 0$ and accordingly set $a = 0$. The minimization interval is then characterized by one parameter b , as for the IC quadrature.⁶

We now discuss how to choose the imaginary time grid. This remains a somewhat involved issue even with the yet gained insight. The main problem is that we want to use one and only one time grid, since this will allow us to represent the Green's functions and the bosonic quantities on the same time grid permitting one to calculate for instance the polarizability as $g(-i\tau)g(+i\tau)$ on that single grid. The even and odd basis functions of the IA and IB ε -isometry in Tab. I are obviously identical for fermions and bosons for positive τ ,

$$\phi(x, \tau) = \frac{1}{2} \frac{\cosh \frac{x}{2}(1 - 2\tau)}{\cosh \frac{x}{2}}, \quad \tau > 0 \quad (22)$$

$$\psi(y, \tau) = \frac{1}{2} \frac{\sinh \frac{y}{2}(1 - 2\tau)}{\cosh \frac{y}{2}}, \quad \tau > 0. \quad (23)$$

Even without considering the related norm in Tab. I, these functions seem to be a handy and intuitive choice, since they can be used to express the diagonal elements

of the free propagator of (1)

$$g_\alpha(-i\tau) = \psi\left(\beta\epsilon_\alpha, \frac{|\tau|}{\beta}\right) + \text{sgn}(\tau)\phi\left(\beta\epsilon_\alpha, \frac{|\tau|}{\beta}\right) \quad (24)$$

as well as the matrix elements of the polarizability (6). Optimization of the time grid for even and odd functions, however, yields different time grids. As already motivated in the previous section, we have decided to use the optimal even time grid (IA₁) as a common grid for both fermionic and bosonic functions and repeat the arguments here. (i) The second order and RPA correlation energy depends only on bosonic functions, e.g. the polarizability. Hence the fermionic functions are only used at an intermediate stage. (ii) The polarizability possesses a special symmetry $\chi(-i\tau) = \chi(-i\beta + i\tau)$ matching the IA₁ ε -isometry in Tab. I. (iii) Finally, the imaginary time grid for the even functions ϕ yields a small minimax error also for the odd basis functions ψ for the entire interval $x \in [0, b]$, with negligible deviations even for $x \rightarrow 0$. This follows from the fact that the corresponding L^2 - norms differ only for very small arguments (compare third column of IA and IB in Tab. I). Consequently, we solve the minimax problem (17) only for $\phi_j(x) = \phi(x, \tau_j) = \langle \tau_j | x \rangle$ and use the same time grid points for the odd basis functions.

To obtain the time grid points τ_j , it is convenient to rewrite the minimax problem (17) into the following form

$$\min_{\sigma_j > 0, \tau_j \in (0, 1/2)} \max_{0 \leq x \leq b} \left| \|x\|_2^2 - \sum_{j=1}^N \sigma_j \phi_j^2(x) \right| \quad (25)$$

with $b = \beta\epsilon_{\max}$ and ϵ_{\max} the maximum one-electron energy considered. Then it becomes evident that (25) is a non-linear fitting problem of separable type,¹⁸ which in general has only a solution, if every basis function ϕ_j is linearly independent and has less than $N - 1$ zeros. The alternant theorem then implies^{12,19} a set of points $\{x_j^*\}_{j=0}^{2N}$ (alternant) and a set of non-linear equations

$$\|x_j^*\|_2^2 - \sum_{k=1}^N \sigma_k^* |\langle \tau_k^* | x_j^* \rangle|^2 = E_N (-1)^j \quad (26)$$

with

$$E_N = \pm \max_{a \leq x \leq b} \left| |\langle \phi | x \rangle|^2 - \sum_{k=1}^N \sigma_k \phi_k(x) \right| \quad (27)$$

being positive (negative) if the l.h.s. of (26) is positive (negative) at $x = x_0^*$.

The alternant theorem provides the basis for the non-linear Remez algorithm that has been used successfully in other papers and yields the minimax solution $\{\sigma_j^*, \tau_j^*\}_{j=1}^N$.^{6,15,16} The minimax solution yields abscissas in the unscaled interval $0 \leq \tau_j^* \leq \frac{1}{2}$. Furthermore, the corresponding weights σ_j^* are positive and $\lim_{N \rightarrow \infty} \sum_{j=1}^N \sigma_j^* = 1$ holds true. This is important for

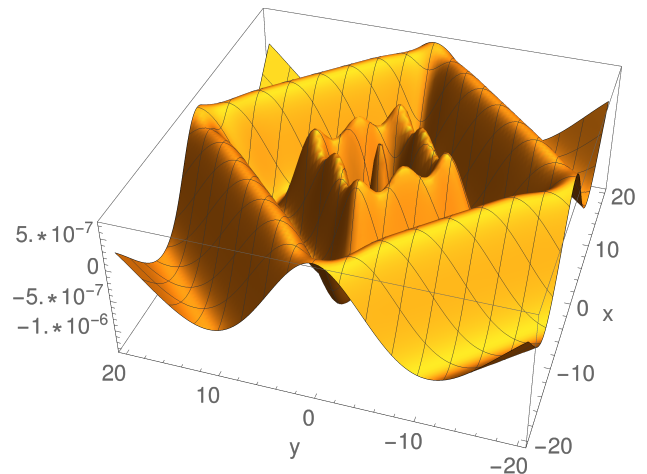


FIG. 3. Time error function [Equ. (28)] of order $N = 6$ for $b = 100$ in two dimensions. For better visibility only the $[-20, 20] \times [-20, 20]$ region of the error surface is shown.

the application in many-body theory, since the conservation of particles is guaranteed with increasing N including particles with energy $\epsilon_\alpha \approx \mu$.

Furthermore, the same minimax quadrature can be used to evaluate "off-diagonal terms", since errors of the form

$$\eta(x, y) = \langle x | y \rangle - \sum_{k=1}^N \sigma_j^* \phi_k^*(x) \phi_k^*(y) \quad (28)$$

are exponentially suppressed with increasing quadrature order N . An example is given in Fig. 3 that demonstrates how the error is uniformly distributed in the entire region $(x, y) \in [a, b] \times [a, b]$ and bounded for $x = y = 0$.

Before we discuss the construction of the frequency grids, we note that a similar basis $e^{-xy} / \cosh \frac{x}{2}$ has been recently used to compress Green's functions on the imaginary time axis in quantum Monte Carlo algorithms.²⁰ We believe that there is a close connection to our method, since we found that the quadrature obtained from the solution of (25) is also a good approximation to the solution for the corresponding problem for the odd basis function (23) and both, ψ and ϕ linear combined yield Shinaoka's basis. However, Shinaoka *et al.* determine the grid as the solution of an integral equation and the connection to ε -isometric subspaces is not immediately evident. We, therefore, prefer to solve the non-linear optimization problem (25) instead.

C. Bosonic Frequency Grid

To construct the bosonic Matsubara grid we use the ε -isometric basis of the even time basis (22), specifically again the IA₁ basis

$$\tilde{\phi}_n(x) = \frac{x}{x^2 + \nu_n^2} \tanh \frac{x}{2}. \quad (29)$$

The motivation behind this choice is three-fold. Firstly, it is obtained from the cosine transformation of the even time basis (22) evaluated for bosonic Matsubara frequencies $\nu_n = 2n\pi$. Thus it describes the imaginary frequency dependence of the polarizability (6) that is of bosonic nature; the IA₂ basis is obtained from the sine transform of these functions and is evaluated at fermionic frequencies and hence irrelevant for the evaluation of bosonic integrals. Secondly, we can use the minimax isometry method to switch between the frequency and time representation of the polarizability with high precision. This follows from the theorem proved in section II Equ. (16). Lastly, the infinite bosonic Matsubara series of the RPA grand potential (B4) can be evaluated with high precision without using any interpolation technique.

In practice, the unscaled bosonic frequency quadrature for $\beta = 1$ is determined first and following scaling relations are used to obtain the result for arbitrary inverse temperatures

$$\nu_k \rightarrow \frac{\nu_k}{\beta}, \quad \lambda_k \rightarrow \frac{\lambda_k}{\beta}. \quad (30)$$

The corresponding minimax problem reads

$$\min_{\lambda_k > 0, \nu_k \in (0, \infty)} \max_{0 \leq x \leq b} \left| \|x\|_2^2 - \sum_{k=1}^N \lambda_k \tilde{\phi}_k^2(x) \right| \quad (31)$$

where the L^2 -norm is given in Tab. I. The solution $\{\lambda_k^*, \nu_k^*\}_{k=1}^N$ is called IA₁-quadrature in the following, in agreement with the notation used in Tab. I.

Before we investigate the convergence of the IA₁-quadrature, we discuss the construction of the fermionic grid.

D. Fermionic Frequency Grid

In this section, we discuss the construction of a compressed fermionic Matsubara quadrature. More precisely, we look for a quadrature that is converging exponentially with the number of grid points N for the GM expression for the grand potential (B5). In contrast to the polarization function and second order correlation energies, this requires an accurate handling of fermionic functions of the type IA₂ and IB₁ in the frequency domain, which is an intricate problem.

First, we consider the frequency dependence of the free propagator (1). The cosine and sine transformations of the odd and even time basis functions (23) and (22) for fermionic frequencies (5) are determined as:

$$\text{IB}_1 : (23) \rightarrow u_m(x) = \langle u_m | x \rangle = \frac{x}{x^2 + \omega_m^2} \quad (32)$$

$$\text{IA}_2 : (22) \rightarrow v_m(x) = \langle v_m | x \rangle = \frac{\omega_m}{x^2 + \omega_m^2}. \quad (33)$$

Then the non-interacting propagator (1) on the fermionic Matsubara axis reads

$$\tilde{g}_\alpha(i\omega_m) = u_m(\epsilon_\alpha - \mu) + iv_m(\epsilon_\alpha - \mu). \quad (34)$$

Second, we observe that every fermionic function can be decomposed into terms that are even and odd in ω , including the product of the propagator and self-energy as it appears in the GM grand potential (B5). It is, obvious, that only the real part of the product $\tilde{G}\tilde{\Sigma}$ contributes to the total energy. Thus the most general matrix element, which gives a non-zero contribution to the GM grand potential has the form²¹

$$\tilde{G}(i\omega_m)\tilde{\Sigma}(i\omega_m) = \sum_{-\Omega_{\max} \leq x, y \leq \Omega_{\max}} A(x)B(y) \times [u_m(x)u_m(y) - v_m(x)v_m(y)], \quad (35)$$

where x and y are the poles of the Green's function and the self-energy on the real-frequency axis and A, B the spectral densities, respectively. Without loss of generality, we set $A = B = 1$ and assume that the magnitudes of the poles are smaller than a positive number, *i.e.* $|x|, |y| \leq \Omega_{\max}$.

Third, we note that the analogue of the IA₁-quadrature of bosonic functions (31) for fermionic ones

$$\min_{\sigma_k > 0, \omega_k \in (0, \infty)} \max_{0 \leq x \leq b} \left| \|x\|_2^2 - \sum_{k=1}^N \sigma_k u_k^2(x) \right| \quad (36)$$

yields the IB₁-quadrature, see Tab.I. Unfortunately, the IB₁-quadrature only allows to evaluate the first term on the r.h.s. of (35) accurately, but fails for the product of two odd functions v . Similarly, the IA₂-quadrature obtained from the minimax problem

$$\min_{\sigma_k > 0, \omega_k \in (0, \infty)} \max_{0 \leq x \leq b} \left| \|x\|_2^2 - \sum_{k=1}^N \sigma_k v_k^2(x) \right| \quad (37)$$

that approximates the same norm as the time and IA₁-quadrature, describes only the second term in (35). Consequently, neither the IB₁- nor the IA₂-quadrature can be used for our purposes.

A solution to this dilemma can be found by approximating the L^1 -norm instead

$$\|x\|_1 = \sum_{m \in \mathbb{Z}} |\langle u_m | x \rangle| = \frac{1}{2} \tanh \frac{|x|}{2}. \quad (38)$$

A proof of this identity is found in the appendix C. That is, we determine the solution of

$$\min_{\gamma_k, \omega_k > 0} \max_{0 \leq x \leq b} \left| \|x\|_1 - \sum_{k=1}^N \gamma_k u_k(x) \right|. \quad (39)$$

Because $\|x\|_2 \leq \|x\|_1$ holds true for any $0 \leq x \leq b$,¹⁰ the L^1 solution $\{\gamma_k^*, \omega_k^*\}_{k=1}^N$, called F-quadrature in the following, yields linearly independent basis functions u_k^* that span a larger vector space than the basis obtained from (36). Our numerical experiments discussed below show that the F-quadrature evaluates the infinite sum over both terms in (35) with high precision for increasing N .

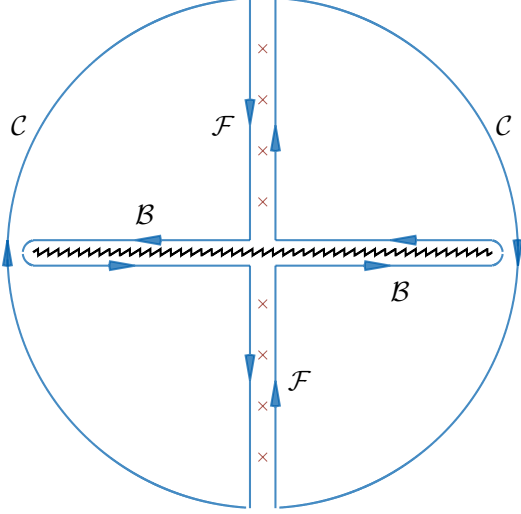


FIG. 4. Integration contours in (43) (zigzag line) branch cut of \tilde{A} , (crosses) fermionic Matsubara frequencies ω_n correspond to poles $z = i\omega_n$ of auxiliary function $h_\eta(z)$ defined in (44) and (45) such that contour integral $\oint_C dz \tilde{A}(z)h_\eta(z)$ for path C is zero.

A similar technique was employed by Ozaki²², who used the same basis functions u , but determined the abscissas from the partial fraction decomposition of the hyperbolic tangent in combination with a continued fraction representation of the hypergeometric function ${}_1F_0$ to derive a compressed form of (38).

Both, the F-quadrature as well as Ozaki's hypergeometric quadrature (OHQ) use essentially a rational polynomial approximation to the hyperbolic tangent. In the following, we show why this approach provides also a good approximation of fermionic Matsubara series, such as the the density matrix for holes (upper sign) and electrons (lower sign)

$$\Gamma = \pm \lim_{\eta \rightarrow 0^\pm} G(-i\eta) = \pm \lim_{\eta \rightarrow 0^\pm} \frac{1}{\beta} \sum_{n=-\infty}^{\infty} \tilde{G}(i\omega_n) e^{-i\omega_n \eta} \quad (40)$$

where G and \tilde{G} is the interacting Green's function in imaginary time and on the Matsubara axis, respectively. Specifically, we show that the last expression on the r.h.s. of (40) can be approximated with the following quadrature formula

$$\Gamma \approx \frac{\text{sgn}(\eta)}{2} \mathbb{1} + \sum_{k=1}^N \frac{\sigma_k}{2} \left[\tilde{G}(i\omega_k) + \tilde{G}(-i\omega_k) \right], \quad (41)$$

where $\mathbb{1}$ is the identity matrix in the considered basis and σ_k, ω_k are either the OHQ- or F-quadrature points.

To understand Equ. (41) and, in general, why an approximation to the hyperbolic tangent provides an excel-

lent approach to compress fermionic Matsubara series, we consider a general correlation function \tilde{A} that is analytic in the complex plane z with a branch cut on the real axis and decays with $\mathcal{O}(|z|^{-1})$ or faster to zero for $|z| \rightarrow \infty$; for instance $\tilde{G}(z)$ or $\tilde{G}(z)\tilde{\Sigma}(z)$. Following Fetter and Walecka,⁴ one introduces an auxiliary function $h_\eta(z)$ with an infinitesimal η to force the complex contour integral over the infinite large outer circle C in Fig. 4 to vanish, that is

$$\oint_C \frac{dz}{2\pi i} \tilde{A}(z)h_\eta(z) = 0. \quad (42)$$

Regardless of the specific choice of $h_\eta(z)$ (discussed below), one can easily show using the residue theorem and the contours depicted in Fig. 4 following identities:

$$\begin{aligned} \sum_{n \in \mathbb{Z}} \text{Res}_{z=i\omega_n} \left[\tilde{A}(z)h_\eta(z) \right] &= \oint_{\mathcal{F}} \frac{dz}{2\pi i} \tilde{A}(z)h_\eta(z) \\ &= - \oint_{\mathcal{B}} \frac{dz}{2\pi i} \tilde{A}(z)h_\eta(z) \\ &= \int_{-\infty}^{\infty} d\omega \frac{1}{\pi} \text{Im} \left[\tilde{A}(\omega)h_\eta(\omega) \right] \end{aligned} \quad (43)$$

Apart from condition (42), the auxiliary function $h_\eta(z)$ has to be chosen such that the l.h.s. in (43) gives the fermionic Matsubara series $\sum_{n \in \mathbb{Z}} \tilde{A}(i\omega_n) e^{-i\omega_n \eta}$, which imposes two conditions on h_η . Firstly, h_η must have an infinite number of poles located at $z = i\omega_n$ (crosses in Fig. 4). Secondly, the corresponding residue has to be $\pm \tilde{A}(i\omega_n) e^{-i\omega_n \eta}$ for $\eta \rightarrow 0^\pm$.

If $\tilde{A}(z)$ is of order $\mathcal{O}(|z|^{-1-\delta})$, $\delta > 0$ for $|z| \rightarrow \infty$ the contour integral (42) is zero also for constant functions $h_\eta(z)$ in η and one can choose

$$\begin{aligned} h_\eta(z) &= \frac{1}{2} \tanh \frac{z}{2} \\ &= \frac{1}{2} \sum_{n \in \mathbb{Z}} \left[\frac{1}{z - i\omega_n} + \frac{1}{z + i\omega_n} \right], \end{aligned} \quad (44)$$

where the last line follows from (38) and shows the locations of the poles of $h_\eta(z)$. Thus for $\tilde{A}(z) = \tilde{G}(z)\tilde{\Sigma}(z)$ the fermionic Matsubara series is independent of the directional limit $\eta \rightarrow 0^\pm$. The replacement of the hyperbolic tangent by a rational polynomial with poles on the imaginary axis in (43) shows that both terms in the GM energy (35) can be well approximated using the F-quadrature.

In contrast, for correlation functions \tilde{A} that decay only with $\mathcal{O}(|z|^{-1})$ at $|z| \rightarrow \infty$ the sign of the infinitesimal η matters. This includes $\tilde{G}(z)$ as well as any mean field terms, *e. g.* Green's function times the mean field Hamiltonian $\tilde{G}(z)H_0$. For instance, the limit $\eta \rightarrow 0^-$ in (40) gives the electron density matrix, while $\eta \rightarrow 0^+$ gives the density matrix of holes. For functions of order $\mathcal{O}(|z|^{-1})$ at $|z| \rightarrow \infty$ one, therefore, has to add a term to the hyperbolic tangent. As can be shown easily, the form for

$h_\eta(z)$ for which (42) holds true is²³

$$h_\eta(z) = \left[\frac{\text{sgn}(\eta)}{2} + \frac{1}{2} \tanh \frac{z}{2} \right] e^{-z\eta}. \quad (45)$$

Inserting Equ. (45) into the r.h.s. of (43) yields

$$\begin{aligned} \sum_{n \in \mathbb{Z}} \tilde{A}(i\omega_n) e^{-i\omega_n \eta} &= \frac{\text{sgn}(\eta)}{2} \int_{-\infty}^{\infty} d\omega \frac{1}{\pi} \text{Im} \left[\tilde{A}(z) e^{-z\eta} \right] \\ &+ \int_{-\infty}^{\infty} d\omega \frac{1}{\pi} \text{Im} \left[\tilde{A}(z) \frac{1}{2} \tanh \frac{z}{2} e^{-z\eta} \right], \end{aligned} \quad (46)$$

In the last term on the r.h.s. the evaluation of the limit $\eta \rightarrow 0$ can be performed before integration, because the integrand is of order $\mathcal{O}(|z|^{-2})$ for $|z| \rightarrow \infty$ [see Equ. (44)]. The corresponding integral over the arch \mathcal{C} vanishes, so that the last term in (46) on the r.h.s. can be rewritten into the Matsubara series of \tilde{A} that is independent of the sign of η . This is the *convergent part* of the Matsubara series and the term that can be evaluated using quadratures. Note that the first term on the r.h.s. of (46) cannot be written into a Matsubara series, because the integrand diverges for $|z| \rightarrow \infty$ prohibiting the closure of the integration contour at infinity. However, for $\tilde{A}(z) = \tilde{G}(z)$ one has

$$\lim_{\eta \rightarrow 0^\pm} \frac{\text{sgn}(\eta)}{2} \int_{-\infty}^{\infty} d\omega \frac{1}{\pi} \text{Im} \left[\tilde{G}(z) e^{-z\eta} \right] = \pm \frac{1}{2} \mathbb{1}. \quad (47)$$

This concludes our proof of Equ. (41). We call this term, therefore, the *divergent part* of the Matsubara series, although the term is finite in any practical calculation (number of electrons/holes is finite in practice). We use (41) for the evaluation of the density matrix in self-consistent *GW* calculations at finite temperature (see section IV).

In summary, one can say that the approximation of the hyperbolic tangent by rational polynomials with poles only on the imaginary axis gives rise to fermionic Matsubara quadratures that describe the convergent part of the Matsubara representation. To obtain the directional limits $\eta \rightarrow 0^\pm$ of weakly decaying correlation functions, such as the propagator of electrons or holes, the integral over the spectral function has to be added or subtracted, respectively. The evaluation of the GM energy does not require this term, because $\tilde{G}(z)\tilde{\Sigma}(z)$ decays with $\mathcal{O}(|z|^{-2})$. Analogous bosonic quadratures can be obtained by approximating the L^1 -norm of the hyperbolic cotangent, but this was not further investigated.

We have compared our F-quadrature with Ozaki's hypergeometric quadrature (OHQ) by means of calculating the GM factor (35) for a model that includes 50 randomly sampled poles in $-0.05 \leq x, y \leq 0.05$ and 50 poles in $-50 \leq x, y \leq 50$. The results for $\beta = 1, 10$ and 100 eV^{-1} are shown in Fig. 5 and are contrasted to the grid convergence for the ordinary fermionic Matsubara quadrature $\{\gamma_m = 2, \omega_m = (2m+1)\pi/\beta\}_{m=0}^\infty$. It can be

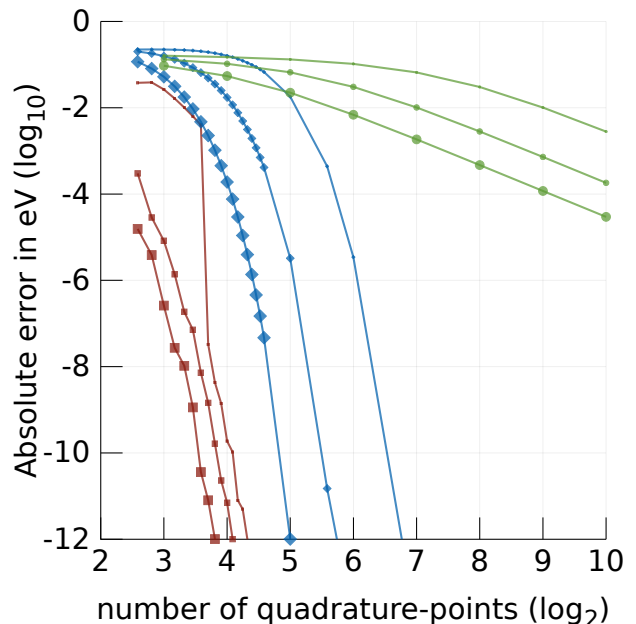


FIG. 5. Convergence of Matsubara grid (points), hypergeometric grid (diamonds) and F-grid (squares) for inverse temperatures $\beta = 1, 10, 100 \text{ eV}^{-1}$ (small, medium, large symbols).

seen that the F-quadrature outperforms the OHQ in all cases, especially for $\beta > 1$ (low temperatures). This can be explained by the fact that the F-grid minimizes the quadrature error for all energies uniformly in the interval $|x|, |y| \leq \Omega_{\text{max}}$. The corresponding OHQ-quadrature error is non-uniformly distributed in the same interval and has the effect that at high β values the convergence is almost linear with the number of grid points for small N . The same figure, also shows the linear convergence of the conventional Matsubara grid and demonstrates its pathology in practice.

E. Minimax Isometry Transformation

We have seen how different basis functions for the time and frequency domain give rise to different grids. In this section we study the error made by transforming an object represented on the time grid $\{\tau_1^*, \dots, \tau_N^*\}$ to the frequency axis. As a measure for the transformation error we use

$$\tilde{E}(\omega) = \min_{t_{\omega k} \in \mathbb{R}} \left\| \langle \omega | x \rangle - \sum_{k=1}^N t_{\omega k} \langle \tau_k^* | x \rangle \right\|_2^2, \quad (48)$$

where $\langle \tau_k^* | x \rangle$ is either the even or odd time basis function (22),(23) evaluated at the minimax time grid obtained from (25) and $\langle \omega | x \rangle$ acts as a placeholder for one of the basis functions in the frequency domain listed in Tab. I with ω being a positive real number. The L^2 -norm is evaluated by sampling the x -values with 100 points X_j^* determined from the alternant $\{x_j^*\}_{j=0}^{2N}$ of the minimax

time problem in (25) and additional $(101 - 2N)/2N$ uniformly distributed points in each of the $2N$ sub-intervals $[x_j^*, x_{j+1}^*]$.

The solution of the ordinary least square problem for the frequency ω is then given by the corresponding normal equation²⁴

$$\sum_{i=1}^{100} \langle \omega | X_i^* \rangle \langle X_i^* | \tau_k^* \rangle = \sum_{j=1}^N t_{\omega_j} \sum_{i=0}^{100} \langle \tau_j^* | X_i^* \rangle \langle X_i^* | \tau_k^* \rangle, \quad k = 1, \dots, N. \quad (49)$$

The transformation error is rather insensitive to changes of the number of sampling points X_j^* ; the $2N + 1$ alternant points x_j^* of the time grid also often suffice in practice.

Furthermore, Equ. (48) allows to plot $\tilde{E}(\omega)$ as a function of the frequency. This gives independent insight, on which frequencies one is supposed to use in combination with a certain set of time basis functions, independent of the previous considerations (see Fig. 6).

Transformation to the IA₁ frequency basis functions (blue line), clearly shows that the error $\tilde{E}(\omega)$ is minimal at the previously determined IA₁ frequency points (blue triangles), and transformation to the IA₂ frequency basis functions (green line) shows that the error is smallest at the previously determined IA₂ frequency points (green diamonds). The reason for this behavior is due to the fact that the IA₁, IA₂ and the time quadrature for the even time basis $\phi(x, \tau)$ [Equ. (22)] possess the same approximation property and span N -dimensional, almost isometric subspaces of the Hilbert space \mathcal{H} as proven in section II. The good agreement is a numerical confirmation that the previously determined frequency grids are optimal.

Thus, for polarizabilities and second order correlation energies, the optimal frequency points are clearly the IA₁-quadrature points (triangles). They approach the conventional bosonic frequencies $2n\pi$ [Equ. (10)] at small ω . The corresponding weights (not shown) approach 2 (except for the first frequency $\nu_1^* = 0$, $\lambda_1^* = 1$). Higher quadrature frequency points (as well as weights) deviate considerably from the conventional bosonic Matsubara points $\{\nu_m = 2\pi m, \lambda_m = 2\}_{m=0}^{\infty}$. This behavior is very similar to the bosonic grid presented by Hu *et al.* that is based on the continued fraction decomposition of the hyperbolic cotangent, the analogue of Ozaki's method for bosons.²⁵ However, the IA₁-quadrature has the advantage that the error is minimized uniformly for all transition energies $|x| \leq \beta\epsilon_{\max}$, while the continued fraction method yields non-uniformly distributed errors in general.

Transformation from the even time basis $\phi(x, \tau)$ [Equ. (22)] to the fermionic frequency basis IA₂ yields further important insight. As already emphasized the minimax IA₂ frequency points match exactly those frequency points where the error for transformation into the IA₂

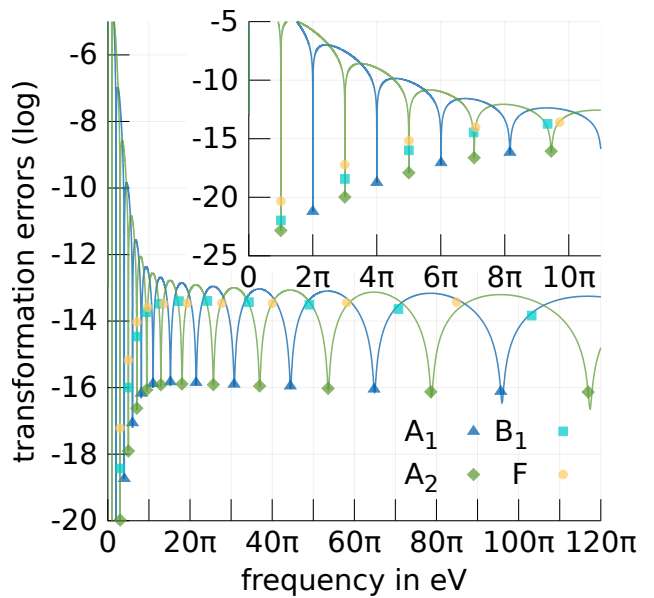


FIG. 6. Transformation error $\tilde{E}(\omega)$ from even time basis functions (22) to the IA₁ (blue) and IA₂ (green) frequency basis for $N = 16$, $x_{\max} = 1000$. The inset shows the low frequency regime. Points indicate minimax grid points in frequency domain for IA₁, IA₂, IB₁ and F (the abscissa corresponds to the optimal frequency, whereas the ordinate is given by the error $\tilde{E}(\omega)$ determined at the respective frequency point).

basis functions is minimal. On the other hand, the IB₁ and F minimax grid points are chosen to optimally present odd time basis functions $\psi(x, \tau)$ [Equ. (23)] using the corresponding frequency basis [Equ. (32)]. At small frequencies, these points are slightly shifted away from the optimal IA₂ frequency points, causing somewhat larger transformation errors for even functions to IA₂ basis functions. This is to be expected, since the points have been chosen to approximate a different scalar product than for IA₂ (and IA₁), see fourth column in Tab. (I). Specifically, the IB₁ minimax frequencies are by construction optimal to present odd time basis functions. Although, IB₁ and IA₂ minimax points are close at low frequencies, they progressively move away at higher frequencies, which prohibits the construction of a common frequency grid that can present the GM energy well (Sec. IID). From this figure, it is somewhat unclear, why the F frequency grid works well, although it is noteworthy that the corresponding frequency points lie roughly at the positions where IA₁ and IA₂ errors intersect. This might implying an equally acceptable representation of odd and even functions.

1. ε -isometric time grids of the F-quadrature

To avoid ambiguity, we call the time grid defined in section IIB the IA time grid in the following, while the

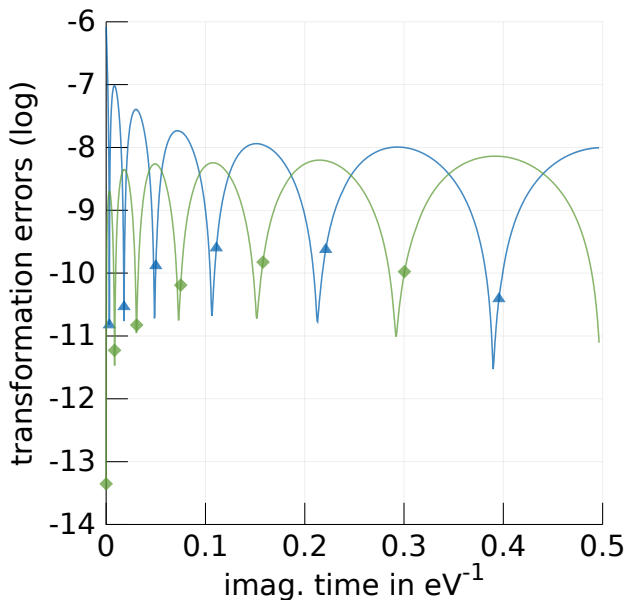


FIG. 7. Transformation error $E(\tau)$ from frequency F-grid to time domain for the IA₂ (blue line) and IB₁ (green line) ε -isometric basis functions in Tab. I for $N = 6$, $x_{\max} = 100$. Triangles and diamonds indicate the IA and IB time grids, respectively.

IB time grid is the same minimax solution (25), but with norm $\|x\|_2$ and basis function $\langle \tau|x \rangle$ of the IB isometry listed in Tab. I.

Recapitulating the previous section, a natural question arises: Is there an optimum time grid for the F-quadrature? In analogy, to Equ. (48) this grid may be defined by the minima of the inverse transformation error

$$E(\tau) = \min_{t_{\tau k} \in \mathbb{R}} \left\| \langle \tau|x \rangle - \sum_{k=1}^N t_{\tau k} \langle \omega_k^*|x \rangle \right\|_2^2, \quad (50)$$

where ω_k^* are the abscissa of the F-quadrature. Table I shows that there are two possible choices for the time and frequency basis functions $\langle \tau|x \rangle$, $\langle \omega_k^*|x \rangle$; one function describing the transformation error from odd to even basis functions (Equ. (33) to Equ. (22)) and one from Equ. (32) to Equ. (23). Both functions are plotted in Fig. 7 (blue and green line), respectively.

The figure clearly shows that the minima of both error functions differ and implies two ε -isometric time grids for the frequency F-grid. This is analogous to the forward transformation errors discussed in the previous section, where the A₁- and A₂-frequency grids are ε -isometric to the IA time grid, respectively. For the F-grid, however, the IA and IB minimax solutions in time coincide with the minima of the error functions only for $\tau \approx 0$, for larger values of τ the transformation error minima (ε -isometric grids) deviate from the IA and IB minimax grid points, respectively (compare minima of green and blue curve with triangles and diamonds in Fig. 7).

The small IB transformation error for $\tau = 0$ follows from the fact that for small τ the time basis becomes $\langle \tau|x \rangle = \psi(x, \tau) \approx \tanh x/2$. Per construction (see (38)), the hyperbolic tangent function is approximated well by the basis (32) using the F-grid. The IA transformation error (blue line), in contrast, is several orders of magnitude larger at $\tau = 0$, since the time basis function is constant $\langle \tau = 0|x \rangle = \phi(x, 0) = 1$ and the frequency basis functions $\langle \omega_k|x \rangle$ represent constants only poorly. The deviation of the IA and IB time grids from the ε -isometric time grids at higher τ values is not surprising, since the F-grid deviates from the ε -isometric frequency grids, that is the A₂ and B₁-grid discussed in section II C and II D.

In summary, we recommend using the IA time grid presented in section II B in combination with the A₁ frequency grid for bosonic functions (see II C) and the F-grid for fermionic functions. First, the exact ε -isometric time points of the F-grid is only known numerically from inspection of the transformation error; an analogue to the minimax isometry method is not known to us. Second, Green's function in imaginary time can be contracted without error, whilst at the same time transformation errors to the imaginary frequency axis are controlled. Before we demonstrate these advantages in section IV, we discuss the following details about our implementation in the Vienna ab initio software package (VASP).²⁶

III. TECHNICAL DETAILS

The implementation of the finite temperature RPA and GW algorithms is the same as the zero-temperature ones,^{7,8} with three exceptions.

- The zero-temperature frequency grid is replaced by the IA₁-grid discussed in II C for the bosonic correlation functions $\tilde{\chi}$, \tilde{W} , while the F-quadrature from II D replaces the grid for the fermionic functions \tilde{G} and $\tilde{\Sigma}$.
- All correlation functions are evaluated on the same imaginary time grid presented in sec. II B.
- The occupied and unoccupied Green's function \underline{G} , \overline{G} need to be set up carefully considering the partial occupancies f_μ in each system.

The last point requires some clarification. The Green's function for positive \overline{G} and negative times \underline{G} can be combined to a full Green's function using Heaviside theta functions

$$G(-i\tau) = \Theta(\tau)\overline{G}(\tau) - \Theta(-\tau)\underline{G}(\tau). \quad (51)$$

At zero temperature ($\beta \rightarrow \infty$) the occupied and unoccupied imaginary time Green's function read^{7,27}

$$\underline{G}(\tau)|_{\beta=\infty} = \sum_{\alpha} \Theta(\epsilon_F - \epsilon_{\alpha}) e^{-(\epsilon_{\alpha} - \epsilon_F)\tau} \quad (52)$$

$$\overline{G}(\tau)|_{\beta=\infty} = \sum_{\alpha} \Theta(\epsilon_{\alpha} - \epsilon_F) e^{-(\epsilon_{\alpha} - \epsilon_F)\tau}. \quad (53)$$

Here the Fermi energy ϵ_F makes sure that \overline{G} and \underline{G} contains only unoccupied (occupied) one-electron states. This changes as temperature increases, which follows from $\lim_{\beta \rightarrow \infty} \mu = \epsilon_F$ and the limit

$$\Theta(\pm\epsilon_F \mp \epsilon_\alpha) = \lim_{\beta \rightarrow \infty} \frac{1}{e^{\pm\beta(\epsilon_\alpha - \mu)} + 1}, \quad (54)$$

implying the form given in (1) for the full Green's function (51). Consequently, the Green's function \underline{G} needs to include also partially occupied states at finite temperature and vice versa, so that the positive and negative imaginary time Green's functions

$$\underline{G}(\tau) = \sum_{\alpha} f_{\alpha} e^{-(\epsilon_{\alpha} - \mu)\tau}, \quad \tau < 0 \quad (55)$$

$$\overline{G}(\tau) = \sum_{\alpha} (1 - f_{\alpha}) e^{-(\epsilon_{\alpha} - \mu)\tau}, \quad \tau > 0 \quad (56)$$

are determined instead and include all considered one-electron states.

We emphasize that for $-\beta \leq \tau \leq \beta$ there are no exponentially growing terms, in neither of the two Green's functions, because of the simple property of the Fermi function

$$f_{\alpha} = (1 - f_{\alpha}) e^{-(\epsilon_{\alpha} - \mu)\beta}. \quad (57)$$

In agreement with the Feynman-Stückelberg interpretation of QFT, every occupied state ($\epsilon_{\alpha} < \mu$) in the positive time Green's function \overline{G} is essentially a state propagating negatively in time

$$(1 - f_{\alpha}) e^{-(\epsilon_{\alpha} - \mu)\tau} = f_{\alpha} e^{-(\epsilon_{\alpha} - \mu)(\tau - \beta)}, \quad 0 < \tau < \beta \quad (58)$$

and vice versa for $\epsilon_{\alpha} > \mu$ and negative times

$$f_{\alpha} e^{-(\epsilon_{\alpha} - \mu)\tau} = (1 - f_{\alpha}) e^{-(\epsilon_{\alpha} - \mu)(\tau + \beta)}, \quad -\beta < \tau < 0. \quad (59)$$

Note, that all time points of the constructed time grid in section (II B) obey $0 < \tau_j < \frac{\beta}{2}$, such that the restrictions for $\tau = \pm\tau_j$ in (58) and (59) are never violated, respectively.

A. Computational details

The results presented in the following section have been obtained with VASP using a Γ -centered k-point grid of $4 \times 4 \times 4$ sampling points in the first Brillouin zone. To be consistent with the QFT formulation Fermi occupancy functions are forced by the code for all finite temperature many-body algorithms (selected with `LFINITE_TEMPERATURE=.TRUE.`), that is `ISMEAR=-1` and the temperature in eV is set via the k-point smearing parameter `SIGMA`. All calculations have been performed with experimental lattice constants of $a = 5.431$ Å for Si²⁸ and $a = 3.842$ Å for SrVO₃²⁹, respectively. For both, Si as well as SrVO₃ the non-normconserving *GW* potentials released with version 5.4.4, specifically

`Si_sv_GW`, `Sr_sv_GW`, `V_sv_GW` and `O_s_GW` have been used and energy cutoffs of 475.1 eV and 434.4 eV for the basis set have been employed, respectively. This allows us to study the grid convergence in the presence of semi-core states and yields results that can be extrapolated to normconserving potentials with higher cutoffs. The independent electron basis required for RPA and *GW* calculations has been determined with density functional theory in combination with the Perdew-Burke-Ernzerhof functional³⁰ and the $q \rightarrow 0$ convergence corrections have been neglected. Furthermore, because the polarizability converges faster with the number of plane waves considered compared to the wavefunction,³¹ smaller energy cutoffs of 316.6 eV and 289.6 eV for χ (set using `ENCUTGW`) for Si and SrVO₃ have been chosen, respectively.

IV. RESULTS

A. Performance of IA₁-quadrature for RPA

We have used the IA₁-quadrature to generalize our cubic scaling RPA algorithm⁷ to finite temperatures in order to calculate the RPA grand potential for SrVO₃ and Si.

We emphasize that in the limit $\beta \rightarrow \infty$ all basis functions approach the IC basis functions used in the zero-temperature RPA algorithms.^{6,32,33} That is at $T=0$ K, the bosonic and fermionic grid merge to the same frequency grid. However, the zero- and finite-temperature grids can be contrasted only for systems with a finite band gap, since the grid convergence of the former breaks down for metallic systems (the L^2 -norm of IC in Tab. I diverges for $x \rightarrow 0$). In contrast, the IA₁-quadrature is valid for all systems (including metals) at all finite temperatures (with exception of the $\beta \rightarrow \infty$ limit). Hence, the Kohn-Luttinger conundrum³⁴ is circumvented, since the thermodynamic limit is performed at finite temperatures. Consequently, a comparison of the grid convergence to our zero temperature implementation of the RPA is useful only for systems with a finite band gap at $T=0$ K, like for instance Si. The corresponding comparisons are given in Fig. 8.

The exponential grid convergence of the IA₁-quadrature for finite temperatures is evident (solid lines). The required number of points for a given precision increases with decreasing temperature, because the minimization interval increases linearly with β and therefore the quadrature error increases too. Not surprisingly, a similar grid convergence rate is observed for paramagnetic SrVO₃ as demonstrated in Fig. 9. This system is known to be computationally challenging, because of the presence of several degenerate, partially populated states around the chemical potential, even in the limit $\beta \rightarrow \infty$.

Comparing the IA₁-convergence rate with the zero temperature grid convergence for Si, a similar slope is observed for $\beta = 100$ eV⁻¹, see empty triangles in Fig.

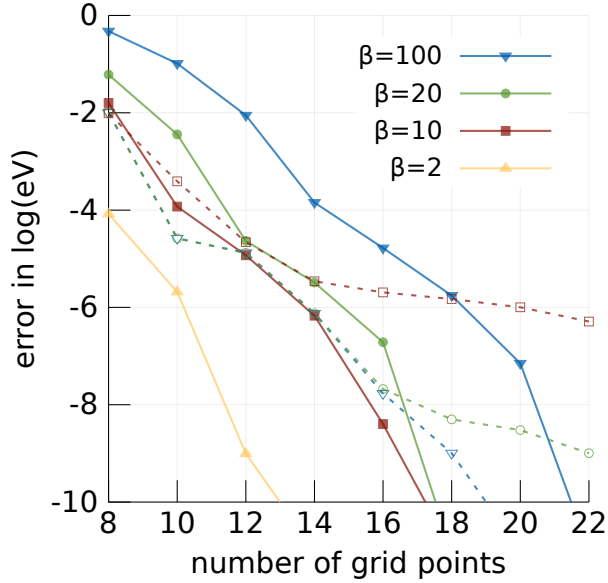


FIG. 8. Grid convergence of RPA grand potential for Si at different temperatures (or k-point smearings). (empty symbols) corresponding $\beta = \infty$ implementation with same k-point smearing applied in the preceding Kohn-Sham groundstate calculation. Inverse temperatures are in eV^{-1} .

8. However, more IA_1 -grid points for the same precision as in the $T = 0$ case are required. The zero temperature quadrature, presented in another work of the authors,⁶ outperforms the finite temperature grid at $\beta = 100 \text{ eV}^{-1}$ corresponding to a sharp k-point smearing of $\beta^{-1} = 0.01 \text{ eV}$. The reason is that the zero temperature grid is "aware" of the band gap and designed to integrate that as well as the largest excitation energies exactly. The finite temperature grid is designed to work between 0 and the largest excitation energy (at a given β). As the temperature increases, partial occupancies are introduced. This has the effect that the exponential convergence rate of the $T = 0$ grid deteriorates and causes the $T = 0$ RPA algorithm even to converge towards a wrong limit that differs from the finite-temperature implementation (not shown). Only for $\beta = 100 \text{ eV}^{-1}$ we observed that both, the zero- and finite-temperature RPA implementations converge to the same result. This is not surprising, because as β becomes smaller more states with energy around ϵ_F become fractionally populated; those states are described incorrectly by the zero-temperature algorithm. Thus, we recommend to use the finite-temperature RPA algorithm for systems with a small or zero band gap.

B. Performance of F-quadrature for GW

Next we study the grid convergence of the F-quadrature for Si and paramagnetic SrVO_3 by means of calculating the GM grand potential in the self-consistent

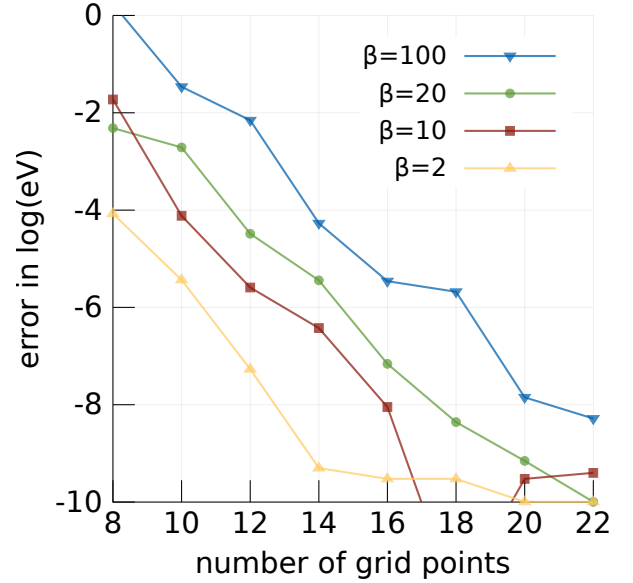


FIG. 9. Grid convergence of RPA grand potential for SrVO_3 at different inverse temperatures. Inverse temperatures are in eV^{-1} .

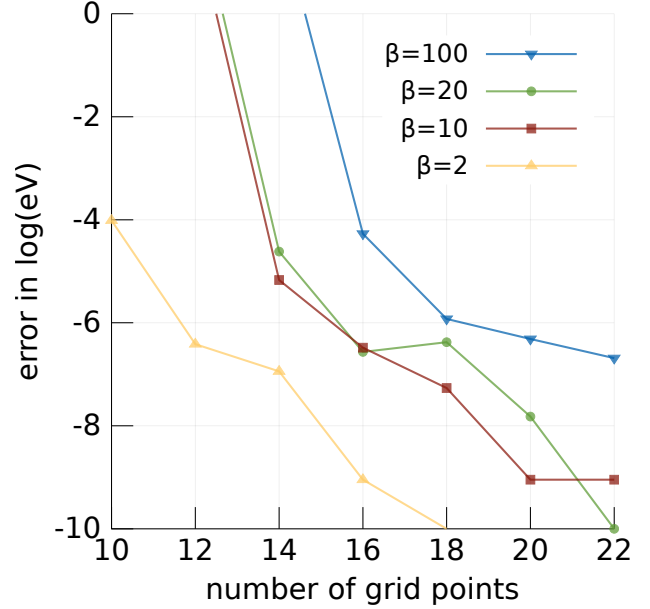


FIG. 10. F-grid convergence for GM grand potential Si. Inverse temperatures are in eV^{-1} .

GW approximation. For demonstration purposes, we have fixed the chemical potential μ in the interacting Green's function (B6) and self-energy to the value of the non-interacting Green's function. Consequently, the interacting Green's function for negative τ describes a system with a different number of electrons N_e in the unit cell than the non-interacting counterpart.³⁵

The results for different values of β of Si and SrVO_3 are

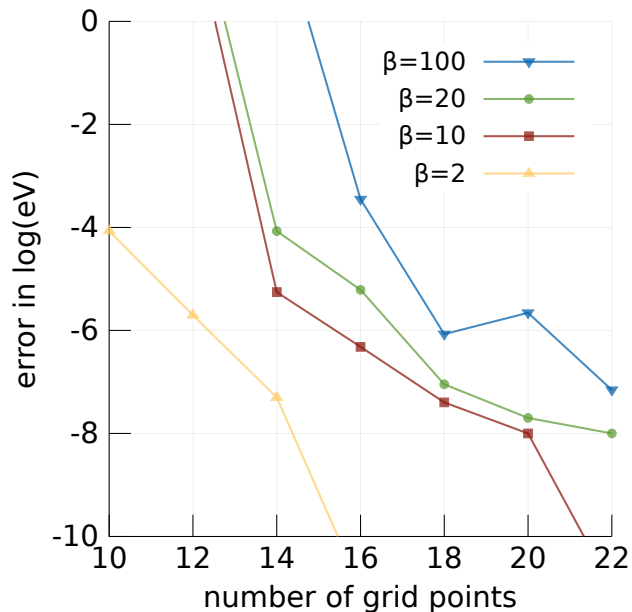


FIG. 11. F-grid convergence for GM grand potential SrVO₃. Inverse temperatures are in eV⁻¹.

given in Fig. 10 and Fig. 11, respectively. One recognizes that the grid convergence is very similar for both systems. Nevertheless, the convergence is worse compared to the RPA, because the F-quadrature error is larger compared to the IA₁-error.

However, our discussion in IIE shows that it is the best choice and the price one has to pay in order to use the same time grid for bosonic and fermionic functions. For practical applications, the error of roughly 1 μ eV with 16 and more quadrature points is negligible. Other convergence parameters, such as the energy cutoff of the basis set, typically yield larger errors.³⁶

Last, we consider the electron number conservation of the F-quadrature, that is the difference of $|N_e - N'_e|$, where N_e is the exact number of electrons in the unit cell and N'_e has been calculated from the trace of Equ. (41). We have studied the non-interacting propagator \tilde{g}_α of SrVO₃. This corresponds to roughly 1056×64 poles of the Green's function on the real-frequency axis in the regime $|x| \leq 400\beta$. The error in the particle number with the number of F-quadrature points is shown in Fig. 12. One can see that the convergence is exponential and increases and decreases with β in the same way as the RPA and GM energies. Not surprisingly, the convergence is the same as compared to the case where the GM energy is used as measure (see Fig. 11). Also, the F-quadrature converges faster with the number of grid points compared to the OHQ-quadrature (not shown). For instance, the F-quadrature yields a precision of 10^{-10} states per unit cell for $\beta = 10$ using $N = 20$ quadrature points, while the same precision is reached with $N = 118$ OHQ-quadrature points.

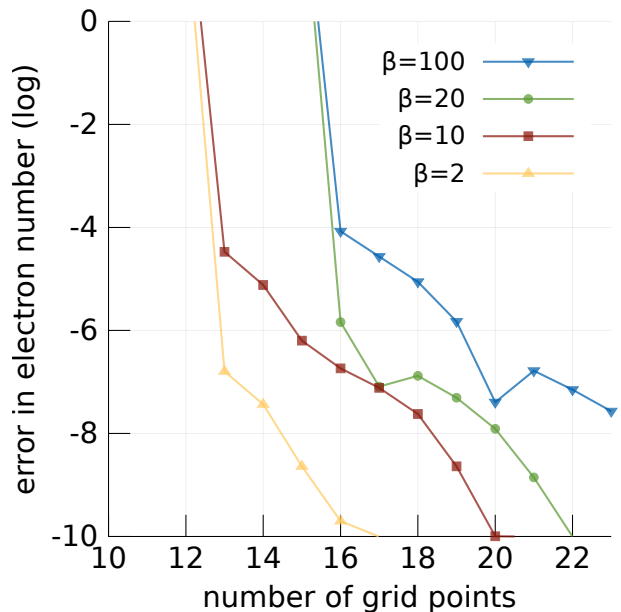


FIG. 12. Particle number conservation error $|N_e - N'_e|$ of F-grid when calculating the electron density from the non-interacting Kohn-Sham propagator of SrVO₃ (see text). Inverse temperatures are in eV⁻¹.

V. CONCLUSION

We presented an efficient method for the Matsubara summation of bosonic and fermionic correlation functions on the imaginary frequency axis. By constructing optimum subspaces of the considered Hilbert space of dimension N , we obtained imaginary time and frequency grids for all correlation functions appearing in finite-temperature perturbation theory. Furthermore, using the argument of ε -isometric spaces, we have shown that the transformation from imaginary time to imaginary frequency can be performed with high precision.

We implemented this technique in VASP to generalize our zero-temperature random phase approximation (RPA) and *GW* algorithms to finite temperatures and obtained a similar exponential grid convergence for the RPA grand potential (see Fig. 8) as in the $T = 0$ case.⁶ To reach μ eV-accuracy, typically, less than 20 grid points are required. This holds true even for low temperatures, so that the RPA grand potential can be evaluated very efficiently for insulating as well as metallic systems with a computational complexity that grows only cubically with the number of electrons in the unit cell.

Furthermore, we showed how to choose the frequency grid for fermionic correlation functions and how to evaluate the Galitskii-Migdal grand potential at finite temperatures using the F-quadrature (see sections IID and IIE). Here a compromise between ε -isometry and integration efficiency has to be made that deteriorates the grid convergence slightly compared to the RPA. For practical applications, however, the precision of the Matsubara

summation is still sufficiently good. Other error sources, such as basis set errors will usually dominate.

In summary, we showed that optimized grids can be found for the accurate Matsubara summation of both, bosonic and fermionic functions, with roughly 20 grid points. The hypergeometric grids of Ozaki²² and Hu *et al.*²⁵ (see section II) require roughly 100 and more points for the same precision at low temperatures and become competitive with our method only at high temperatures (where $\beta \geq 1$).

Appendix A: Finite Temperature Formalism of Quantum Field Theory

This paper follows closely the formalism used in the book of Negele and Orland.³ We consider a system in thermal equilibrium, where the total number of particles is constant (electrons and holes). In contrast the number of electrons (or holes) depends on the chemical potential μ , so that the system is described by the grand canonical ensemble with following partition function

$$Z = \text{Tr} \left\{ e^{-\beta(\hat{H} - \mu\hat{N})} \right\} \quad (\text{A1})$$

and the corresponding grand potential

$$\Omega = -\frac{1}{\beta} \ln Z. \quad (\text{A2})$$

Here the trace is performed w.r.t. an orthonormal basis of the full many-body Hamiltonian \hat{H}

$$\hat{H} = \hat{H}_0 + \hat{V} \quad (\text{A3})$$

containing the Coulomb repulsion of all electrons \hat{V} , the particle number operator \hat{N} and the non-interacting part \hat{H}_0 that can be expressed as sum of one-electron Hamiltonians \hat{h}_i . For the present paper, the exact form of \hat{h}_i does not matter.³⁷ We only assume that we have access to the one-electron eigensystem $\{|\varphi_\alpha\rangle, \epsilon_\alpha\}$ of \hat{h}_i and, thus, can determine the solutions of the non-interacting eigenvalue problem

$$\hat{H}_0|\Phi_A\rangle = E_A|\Phi_A\rangle, \quad (\text{A4})$$

from a linear combination of Hartree products (Einstein summation assumed)

$$\Phi_A(\mathbf{r}_1, \dots, \mathbf{r}_M) = c^{\alpha_1 \dots \alpha_M} \varphi_{\alpha_1}(\mathbf{r}_1) \dots \varphi_{\alpha_M}(\mathbf{r}_M) \quad (\text{A5})$$

The non-interacting solutions $|\Phi_A\rangle$, where A numbers different (but orthogonal) eigenvalues of \hat{H}_0 provide a basis for our calculations and allow to write the number operator \hat{N} and \hat{H}_0 in second quantization as

$$\hat{H}_0 = \sum_{\alpha} \epsilon_{\alpha} \hat{a}_{\alpha}^{\dagger} \hat{a}_{\alpha} \quad (\text{A6})$$

$$\hat{N} = \sum_{\alpha} \hat{a}_{\alpha}^{\dagger} \hat{a}_{\alpha}. \quad (\text{A7})$$

Furthermore, the non-interacting density operator

$$\hat{\rho}_0 = e^{-\beta(\hat{H}_0 - \mu\hat{N} - \Omega_0)} \quad (\text{A8})$$

and the non-interacting grand potential

$$\begin{aligned} \Omega_0 &= -\frac{1}{\beta} \ln Z_0 \\ &= -\frac{1}{\beta} \ln \sum_A \langle \Phi_A | e^{-\beta(\hat{H}_0 - \mu\hat{N})} | \Phi_A \rangle \\ &= \frac{1}{\beta} \sum_{\alpha} \ln f_{\alpha}, \end{aligned} \quad (\text{A9})$$

provides access to expectation values of observables in the non-interacting system, such as the averaged number of electrons in state $|\varphi_{\alpha}\rangle$ at a given temperature $T = \beta^{-1}$ (measured in units of eV)

$$f_{\alpha} = \text{Tr} \left\{ \hat{\rho}_0 \hat{a}_{\alpha}^{\dagger} \hat{a}_{\alpha} \right\} = \frac{1}{e^{\beta(\epsilon_{\alpha} - \mu)} + 1}. \quad (\text{A10})$$

Introducing thermal averages of an operator $\hat{\mathcal{O}}$ w.r.t. to the non-interacting system

$$\langle \hat{\mathcal{O}} \rangle_{\beta} = \sum_A \langle \Phi_A | \hat{\rho}_0 \hat{\mathcal{O}} | \Phi_A \rangle, \quad (\text{A11})$$

the Gell-Mann and Low theorem³⁸ can be used to relate all observables in the interacting system to the non-interacting one. More about this can be found in various books.^{3,4,39} For this paper, only the interacting grand potential is relevant

$$\Omega = \Omega_0 + \Omega_v \quad (\text{A12})$$

$$\Omega_v = -\frac{1}{\beta} \ln \left\langle \hat{T}_{\tau} e^{-\int_{-\frac{\beta}{2}}^{\frac{\beta}{2}} d\tau \hat{V}(-i\tau)} \right\rangle_{\beta} \quad (\text{A13})$$

Here the interacting part Ω_v is expressed using the interaction picture (Heisenberg picture in imaginary time)³⁹

$$\hat{V}(-i\tau) = e^{\beta(\hat{H}_0 - \mu\hat{N})} \hat{V} e^{-\beta(\hat{H}_0 - \mu\hat{N})}, \quad (\text{A14})$$

the imaginary time ordering operator

$$\hat{T}_{\tau} \hat{A}(\tau) \hat{B}(0) = \begin{cases} \hat{A}(\tau) \hat{B}(0), & \tau > 0 \\ -\hat{B}(0) \hat{A}(\tau), & \tau < 0 \end{cases} \quad (\text{A15})$$

and the Coulomb operator \hat{V} in second quantization with the matrix elements

$$V_{\alpha\alpha'\gamma\gamma'} = \left\langle \varphi_{\alpha}, \varphi_{\gamma} \left| \frac{1}{|\mathbf{r} - \mathbf{r}'|} \right| \varphi_{\gamma'}, \varphi_{\alpha'} \right\rangle. \quad (\text{A16})$$

All approximations to the grand potential follow from an expansion of the exponential in (A13) and summation of specific terms. If one uses the prescription of Feynman diagrams to describe these terms, the natural logarithm in (A13) makes sure that only topologically connected diagrams contribute to the approximation (linked cluster theorem).

Appendix B: Approximations to the grand potential

Consider for instance the second order direct Møller-Plessett contribution to the grand potential

$$\Omega_c^{\text{MP2}} = \frac{1}{2} \int_{-\frac{\beta}{2}}^{\frac{\beta}{2}} d\tau_1 \int_{-\frac{\beta}{2}}^{\frac{\beta}{2}} d\tau_2 \quad (\text{B1})$$

$$\times \text{Tr} \{ \chi(-i\tau_1 + i\tau_2) \mathbf{V} \chi(-i\tau_2 + i\tau_1) \mathbf{V} \},$$

where $\chi(-i\tau_1 + i\tau_2) \mathbf{V}$ indicates the matrix multiplication with the Coulomb matrix elements (A16) and the trace is performed over the one-electron indices. Analyzing the integrand in (B1), shows that no exponentially growing terms appear, since the imaginary time arguments always stay inside the fundamental interval $(-\beta, \beta)$. This also holds true for so-called metallic contributions, which are terms with $|\epsilon_\alpha - \epsilon_\gamma| \rightarrow 0$. Proper inspection of these terms shows that they are proportional to the inverse temperature of the system β and only diverge as the temperature approaches 0 K.

Expression (B1) can be generalized to higher orders. For instance the contribution of order k (k -th order ring diagram) contains k convolutions in τ and is of the form

$$\Omega_c^k \propto \frac{1}{k} \int_{-\frac{\beta}{2}}^{\frac{\beta}{2}} d\tau_1 \cdots \int_{-\frac{\beta}{2}}^{\frac{\beta}{2}} d\tau_k \quad (\text{B2})$$

$$\times \chi(-i\tau_1 + \tau_2) \mathbf{V} \chi(-\tau_2 + i\tau_3) \mathbf{V} \cdots$$

$$\cdots \chi(-i\tau_k + i\tau_1) \mathbf{V}.$$

Here the Matsubara method shows its advantage, because it exploits the convolution theorem of harmonic analysis. A convolution in time, becomes a product in Fourier space and vice versa. Applying this theorem to (B2) results in a single series over Matsubara frequencies

$$\Omega_c^k = \frac{1}{\beta} \sum_{n \in \mathbb{Z}} \frac{1}{k} \text{Tr} \{ \tilde{\chi}(i\nu_n) \mathbf{V} \}^k. \quad (\text{B3})$$

Similarly other approximated expressions of observables in euclidean QFT are tremendously simplified. In the following we discuss two well-known approximations to the correlation part of the grand potential. That is the random phase (RPA) and GW approximation.

The RPA can be understood as an infinite sum of all possible ring diagrams (contribution of the form (B3)) that becomes exact for the correlation energy of the interacting homogeneous electron gas at very high density as $T \rightarrow 0$.⁴⁰⁻⁴³ A closed form of the grand potential in the RPA can be found in Negele and Orland's book³ and reads

$$\Omega_c^{\text{RPA}} = \frac{1}{\beta} \sum_{n \in \mathbb{Z}} \text{Tr} \{ \ln [\mathbb{1} - \tilde{\chi}(i\nu_n) \mathbf{V}] - \tilde{\chi}(i\nu_n) \mathbf{V} \} \quad (\text{B4})$$

This expression stands for a typical Fourier series over bosonic frequencies and will provide a measure to test the IA₁-grid convergence in section IV.

The RPA is an approximative bosonization of the original problem. As an example of methods where bosonization is typically not applicable, we decided to evaluate the GM expression⁴⁴ for correlation part of the grand potential

$$\Omega_c^{\text{GM}} = \frac{1}{\beta} \sum_{m \in \mathbb{Z}} \text{Tr} \left[\tilde{\mathbf{G}}(i\omega_m) \tilde{\mathbf{\Sigma}}(i\omega_m) \right]. \quad (\text{B5})$$

Here $\tilde{\mathbf{G}}$ is the GW dressed propagator and the solution of the Dyson equation

$$\tilde{\mathbf{G}}(i\omega_m) = \tilde{\mathbf{g}}(i\omega_m) + \tilde{\mathbf{g}}(i\omega_m) \tilde{\mathbf{\Sigma}}(i\omega_m) \tilde{\mathbf{G}}(i\omega_m) \quad (\text{B6})$$

where \mathbf{g} is the Hartree propagator (or Hartree Green's function), $\tilde{\mathbf{\Sigma}}$ the GW self-energy

$$\tilde{\mathbf{\Sigma}}(i\omega_m) = \int_{-\beta/2}^{\beta/2} d\tau \mathbf{G}(-i\tau) \mathbf{W}(-i\tau) e^{i\omega_m \tau} \quad (\text{B7})$$

and $\tilde{\mathbf{W}}$ the RPA screened potential

$$\tilde{\mathbf{W}}(i\nu_n) = \tilde{\mathbf{V}} + \tilde{\mathbf{V}} \tilde{\chi}(i\nu_n) \tilde{\mathbf{W}}(i\nu_n). \quad (\text{B8})$$

Appendix C: Poisson summation and hyperbolic functions: A proof of Equ. (38)

To proof identity (38), we use Poissons summation formula⁴⁵

$$\sum_{n \in \mathbb{Z}} f(n) = \sum_{k \in \mathbb{Z}} \tilde{f}(k) \quad (\text{C1})$$

for a function $f(t)$ and its Fourier transform $\tilde{f}(k)$. Inserting $f(tz) = e^{-2|tz|}$ into the l.h.s. of (C1) one obtains with the geometric series the hyperbolic cotangent

$$\sum_{n \in \mathbb{Z}} e^{-2|nz|} = \frac{1 + e^{-2|z|}}{1 - e^{-2|z|}} = \coth |z|. \quad (\text{C2})$$

Consequently, evaluating the Fourier integral gives

$$\tilde{f}(k) = \int_{-\infty}^{\infty} dt e^{-2|tz|} e^{i2\pi kt} = \frac{|z|}{\pi^2 k^2 + |z|^2}, \quad (\text{C3})$$

which after inserting into the r.h.s. of (C1) yields the identity

$$\coth |z| = \sum_{k \in \mathbb{Z}} \frac{|z|}{\pi^2 k^2 + |z|^2}. \quad (\text{C4})$$

On the one hand, replacing $|z| \rightarrow |z|/2$ and dividing by 2, this identity becomes

$$\frac{1}{2} \coth \frac{|z|}{2} = \sum_{k \in \mathbb{Z}} \frac{|z|}{(\pi 2k)^2 + |z|^2}. \quad (\text{C5})$$

On the other hand, the series (C4) on the r.h.s. can be split into a series over even and a series over odd integers

$$\coth |z| = \underbrace{\sum_{k \in \mathbb{Z}} \frac{|z|}{(\pi 2k)^2 + |z|^2}}_{=\frac{1}{2} \coth \frac{|z|}{2}} + \sum_{k \in \mathbb{Z}} \frac{|z|}{(\pi(2k+1))^2 + |z|^2} \quad (\text{C6})$$

The first term on the r.h.s. follows from (C5), while the second part is the l.h.s. of Equ. (38). After comparison

with the well-known hyperbolic identity

$$\coth z = \frac{1}{2} \coth \frac{z}{2} + \frac{1}{2} \tanh \frac{z}{2}, \quad (\text{C7})$$

one identifies the second term in (C6) with

$$\frac{1}{2} \tanh \frac{|z|}{2} = \sum_{k \in \mathbb{Z}} \frac{|z|}{(\pi(2k+1))^2 + |z|^2} \quad (\text{C8})$$

and Equ. (38) is proven.

Note that the derivative of the l.h.s and r.h.s. of Eqs. (C8) and (C5) gives an alternative way to calculate the L^2 -norms tabulated in Tab. I.

-
- * merzuk.kaltak@vasp.at; VASP Software GmbH, Sensengasse 8/17, A-1090 Wien, Austria
- † georg.kresse@univie.ac.at; University of Vienna, Faculty of Physics and Center for Computational Materials Science, Universität Wien, Sensengasse 8/8-12, A-1090 Wien, Austria
- ¹ G. C. Wick, Phys. Rev. **96**, 1124 (1954).
 - ² T. Matsubara, Progress of Theoretical Physics **14**, 351 (1955).
 - ³ J. Negele and H. Orland, *Quantum many-particle systems*, Frontiers in physics (Addison-Wesley Pub. Co., 1988).
 - ⁴ A. L. Fetter and J. D. Walecka, *Quantum theory of many-particle systems*, Dover Books on Physics (Dover Publications, 2003).
 - ⁵ F. W. J. Olver, A. B. Olde Daalhuis, D. W. Lozier, B. I. Schneider, R. F. Boisvert, C. W. Clark, B. R. Miller, and B. V. Saunders, “NIST digital library of mathematical functions,” .
 - ⁶ M. Kaltak, J. Klimeš, and G. Kresse, Journal of Chemical Theory and Computation **10**, 2498 (2014).
 - ⁷ M. Kaltak, J. Klimeš, and G. Kresse, Phys. Rev. B **90**, 054115 (2014).
 - ⁸ P. Liu, M. Kaltak, J. Klimeš, and G. Kresse, Phys. Rev. B **94**, 165109 (2016).
 - ⁹ The isometry (13) is known as Parseval theorem¹³ or, if $|n\rangle$ is continuous, Plancherel theorem for Fourier transforms.⁴⁶
 - ¹⁰ R. Fleming and J. Jamison, *Isometries on Banach Spaces: function spaces* (CRC Press, 2002).
 - ¹¹ G. Ding, Acta Mathematica Scientia **8**, 361 (1988).
 - ¹² D. Braess, *Nonlinear Approximation Theory* (Springer-Verlag, 1986).
 - ¹³ B. von Querenburg, *Mengentheoretische Topologie* (Springer Berlin Heidelberg, 2013).
 - ¹⁴ S. Axler, H. Schaefer, M. Wolff, M. Wolff, F. Gehring, and K. Ribet, *Topological Vector Spaces* (Springer New York, 1999).
 - ¹⁵ D. Braess and W. Hackbusch, IMA Journal of Numerical Analysis **25**, 685 (2005).
 - ¹⁶ A. Takatsuka, S. Ten-No, and W. Hackbusch, The Journal of chemical physics **129**, 044112 (2008).
 - ¹⁷ M. Grumet, P. Liu, M. Kaltak, J. Klimeš, and G. Kresse, Phys. Rev. B **98**, 155143 (2018).
 - ¹⁸ G. Golub and V. Pereyra, Inverse Problems **19**, R1 (2003).
 - ¹⁹ G. Hammerlin and K. Hoffmann, *Numerische Mathematik* (Springer Berlin Heidelberg, 1994).
 - ²⁰ H. Shinaoka, J. Otsuki, M. Ohzeki, and K. Yoshimi, Phys. Rev. B **96**, 035147 (2017).
 - ²¹ The imaginary part is proportional to odd terms in the frequency $u_m(\epsilon_\alpha)v_m(\delta_\gamma) + v_m(\epsilon_\alpha)u_m(\delta_\gamma)$ and vanishes when the sum over all (positive and negative) fermionic Matsubara frequencies is carried out.
 - ²² T. Ozaki, Phys. Rev. B **75**, 035123 (2007).
 - ²³ Note, this expression is obtained from the free propagator (1) by replacing $\epsilon_\alpha - \mu \rightarrow z$, $\tau \rightarrow \eta$ and using the identity $f(z) = \frac{1}{2} - \frac{1}{2} \tanh \frac{z}{2}$.
 - ²⁴ W. H. Press, S. A. Teukolsky, W. T. Vetterling, and B. P. Flannery, *Numerical Recipes 3rd Edition: The Art of Scientific Computing* (Cambridge University Press, 2007).
 - ²⁵ J. Hu, R.-X. Xu, and Y. Yan, The Journal of Chemical Physics **133**, 101106 (2010).
 - ²⁶ G. Kresse and D. Joubert, Phys. Rev. B **59**, 1758 (1999).
 - ²⁷ H. N. Rojas, R. W. Godby, and R. J. Needs, Phys. Rev. Lett. **74**, 1827 (1995).
 - ²⁸ M. Levinstein, S. Rumyantsev, and M. Shur, *Handbook Series on Semiconductor Parameters* (World Scientific, London, 1999).
 - ²⁹ M. Onoda, H. Ohta, and H. Nagasawa, Solid State Communications **79**, 281 (1991).
 - ³⁰ J. P. Perdew, M. Ernzerhof, and K. Burke, J. Chem. Phys. **105**, 9982 (1996).
 - ³¹ J. Harl and G. Kresse, Phys. Rev. B **77**, 045136 (2008).
 - ³² B. Helmich-Paris and L. Visscher, Journal of Computational Physics **321**, 927 (2016).
 - ³³ M. Beuerle, D. Graf, H. F. Schurkus, and C. Ochsenfeld, The Journal of Chemical Physics **148**, 204104 (2018), <https://doi.org/10.1063/1.5025938>.
 - ³⁴ W. Kohn and J. M. Luttinger, Phys. Rev. **118**, 41 (1960).
 - ³⁵ Fixing this requires the adjustment of the chemical potential and re-calculation of the interacting Green’s function G until $N_e = \lim_{\tau \rightarrow 0^-} \text{Tr}G(-i\tau)$ is satisfied.
 - ³⁶ J. Klimeš, M. Kaltak, and G. Kresse, Phys. Rev. B **90**, 075125 (2014).
 - ³⁷ In textbooks the non-interacting term \hat{H}_0 is usually the Hartree-Fock Hamiltonian, which has the advantage that several so-called abnormal diagrammatic contributions to the total energy vanish³. In practice, however, one typically uses the DFT Hamiltonian where those contributions are

- small but non-zero.⁴⁷
- ³⁸ M. Gell-Mann and F. Low, Phys. Rev. **84**, 350 (1951).
- ³⁹ A. Abrikosov, L. Gorkov, I. Dzyaloshinski, and R. Silverman, *Methods of Quantum Field Theory in Statistical Physics*, Dover Books on Physics (Dover Publications, 2012).
- ⁴⁰ M. Gell-Mann and K. A. Brueckner, Phys. Rev. **106**, 364 (1957).
- ⁴¹ D. Bohm and D. Pines, Phys. Rev. **82**, 625 (1951).
- ⁴² D. Pines and D. Bohm, Phys. Rev. **85**, 338 (1952).
- ⁴³ D. Bohm and D. Pines, Phys. Rev. **92**, 609 (1953).
- ⁴⁴ F. Caruso, D. R. Rohr, M. Hellgren, X. Ren, P. Rinke, A. Rubio, and M. Scheffler, Phys. Rev. Lett. **110**, 146403 (2013).
- ⁴⁵ J. R. Higgins, Bull. Amer. Math. Soc. (N.S.) **12**, 45 (1985).
- ⁴⁶ M. Plancherel, Rendiconti del Circolo Matematico di Palermo (1884-1940) **30**, 289 (1910).
- ⁴⁷ J. Klimeš, M. Kaltak, E. Maggio, and G. Kresse, The Journal of Chemical Physics **143**, 102816 (2015).